Complex and real unconventional Bose-Einstein condensations in high orbital bands

Zi Cai and Congjun Wu

Department of Physics, University of California, San Diego, California 92093, USA

(Received 15 June 2011; revised manuscript received 1 September 2011; published 26 September 2011)

We perform a theoretical study on the recently observed unconventional Bose-Einstein condensations (UBEC) in the high bands of optical lattices. These exotic states are characterized by complex-valued condensate wave functions with nodal points or real-valued wave functions with nodal lines; thus, they are beyond the "*no-node*" theorem of conventional BECs. A quantum phase transition is driven by the competition between the single-particle band and interaction energies. The complex UBECs spontaneously break time-reversal symmetry, exhibiting a vortex-antivortex lattice structure.

DOI: 10.1103/PhysRevA.84.033635 PACS number(s): 03.75.Nt, 03.75.Lm, 05.30.Jp, 05.30.Rt

Quantum wave functions are generally complex-valued. However, the usual ground state wave functions of bosons are very restricted because they are positive definite, as stated in the "*no-node*" theorem [1]. This theorem applies under very general conditions: the kinetic energy is unfrustrated (e.g. the Laplacian type), the single particle potential can be arbitrary, and the two-body interaction depends only on coordinates. Mathematically, it is a direct consequence of the Perron-Frobenius theorem of matrix analysis [2]. This theorem implies that time-reversal (TR) symmetry cannot be spontaneously broken in various ground states of bosons, including superfluid, Mott-insulating, and supersolid states.

The "*no-node*" theorem, however, only applies to the ground state and hence not to metastable excited states of bosons. This opens up a possibility for "unconventional" states of bosons beyond the "*no-node*" theorem [3]. Similarly to unconventional superconductors, in unconventional Bose-Einstein condensation (UBEC), the condensate wave functions form nontrivial representations of the lattice symmetry groups. However, a major difference exists. Cooper pairs have the center-of-mass motion and the relative motion between the two electrons of the pair. In unconventional superconductors, it is the relative motion that is nontrivial. The degree of freedom of the relative motion does not exist in the single-boson BEC. In UBECs, the condensate wave functions are nontrivial.

Considerable efforts have been made to study unconventional states of bosons, both experimentally and theoretically. Among the most exciting achievements are the realizations of metastable excited states of bosons in high orbital bands [4–7], which lead to the opportunity to study UBEC [8–15] and other exotic properties [16–21]. Below are some recent experimental results. Sebby-Strabley *et al.* succeeded in pumping a large fraction of bosons into the excited bands in a double-well lattice [4]. Mueller *et al.* observed the quasi-one-dimensional phase coherence pattern by exciting bosons into the p orbital bands in a cubic lattice [5]. Important progress was made by the group of Hemmerich [6]: UBEC in sp-hybridized orbital bands were realized in a checkerboard-like lattice, which allows the establishment of fully cross-dimensional coherence. More recently, UBEC in even higher orbital bands has been observed by the same group [7].

In this paper, we present a theoretical study of UBEC observed in the second- or first-excited band of the checkerboard optical lattice. This band is of a hybridized nature between the s orbitals of the shallower sites and the p orbitals of the deeper sites. The lattice asymmetry favors a real-valued condensate wave function with nodal lines, while interactions favor a complex-valued one with nodal points. By solving the Gross-Pitaevskii (GP) equation for these metastable condensates, we find that tuning the lattice asymmetry drives the phase transition between these two types of UBEC, in a good agreement with experimental observations.

We now introduce the optical lattice employed in the experiment [6]. Each unit cell consists of two sites with different depths (denoted A and B below) as shown in Fig. 1(a). (A similar lattice potential with different parameters is plotted in Ref. [6]). The lattice is constructed by the interference pattern of phase-coherent laser beams along the $\pm x$ and $\pm y$ directions generated from a single laser through beam splitters and reflectors. The optical potential reads

$$V(x,y) = -\frac{V_0}{4}|(\hat{z}\cos\alpha + \hat{y}\sin\alpha)e^{ik_l x} + \epsilon\hat{z}e^{-ik_l x} + \eta e^{i\theta}\hat{z}(e^{ik_l y} + \epsilon e^{-ik_l y})|^2, \quad (1)$$

where $\hat{y}$ and $\hat{z}$ are unit vectors describing light polarizations, k_l is the laser wave vector, $\epsilon < 1$ and $\eta < 1$ describe the imperfect reflection and transmission efficiencies, respectively, θ is the phase difference between beams along the x and y directions, and α is used to tune the lattice asymmetry by rotating the light polarization out of the $\hat{z}$ direction.

The point group symmetry of this lattice is analyzed below. We start from the ideal case of $\epsilon = 1$ with $\alpha = 0^\circ$ and $\theta = 90^\circ$, for which the A and B sites are equivalent. For $\eta < 1$, the lattice has the reflection symmetries with respect to both the x and y axes; thus, the lattice is orthorhombic. Next, we keep $\epsilon = 1$ and $\alpha = 0^\circ$ but set θ away from 90°. In this case, the unit cell includes both A and B sites. The primitive lattice vectors are $a_0(\hat{e}_x \pm \hat{e}_y)$, where $a_0 = \pi/k_l$ as shown in Fig. 1(b). The optical potential becomes $V = -\frac{V_0}{2}(\cos 2k_l x + \eta^2 \cos 2k_l y + 4\eta\cos\theta\cos k_l x \cos k_l y)$. The quantity θ controls the potential difference between A and B sites. The point group symmetry remains orthorhombic.

Now we move to the realistic case of $\epsilon < 1$. The unit cell remains double-well shaped and the primitive lattice vectors are the same. However, the orthorhombic symmetry is broken and there is no point group symmetry for general values of parameters. This asymmetry can be partially compensated by setting $\alpha_0 = \cos^{-1}\epsilon$. We

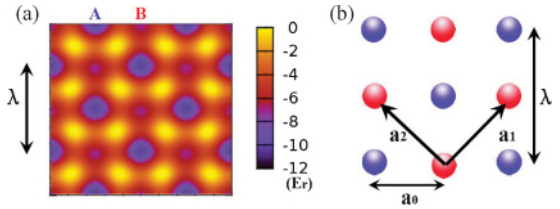

FIG. 1. (Color online) (a) Optical lattice with reflection symmetry with respect to the x axis and parameter values: $\eta = 0.95$, $\epsilon = 0.81$, $\theta = 95.4^\circ$, $\alpha = \alpha_0 = 36^\circ$, and $V_0 = 6.2E_r$. The A sites have deeper potential depth than the B sites. (b) Basis vectors of double-well lattice.

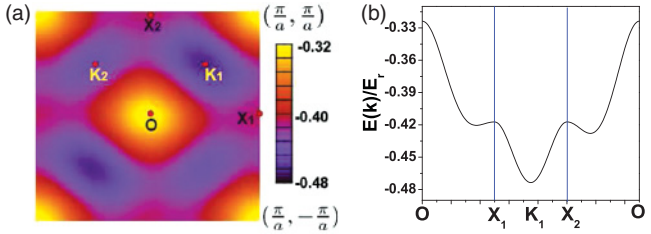

FIG. 2. (Color online) (a) Energy spectrum for second band. The parameter values are the same as for Fig. 1 except that $\alpha = 0^\circ$. (b) Spectrum of (a) along line from $(0, \frac{\pi}{a})$ to $(\frac{\pi}{a}, 0)$.

denote this configuration as "symmetric" and the other ones with $\alpha \neq \alpha_0$ as "asymmetric." The symmetric lattice potential becomes $V = -\frac{V_0}{2}\epsilon(\epsilon \cos 2k_l x + \eta^2 \cos 2k_l y) - V_0\eta\epsilon \cos k_l x[\cos(k_l y + \theta) + \epsilon^2 \cos(k_l y - \theta)]$, which has reflection symmetry with respect to the x axis but not with respect to the y axis.

Next, we calculate the band structures. The reciprocal lattice vectors are defined as $\vec{G}_{m,n} = m\vec{b}_1 + n\vec{b}_2$ with $\vec{b}_{1,2} = (\pm\frac{\pi}{a}, \frac{\pi}{a})$. The single-particle Hamiltonian reads $H_0 = -\hbar^2\vec{\nabla}^2/(2M) + V(r)$, where M is the boson mass. Using the plane wave basis, the diagonal matrix elements are $\langle\vec{k} + \vec{G}_{mn}|H_0|\vec{k} + \vec{G}_{mn}\rangle = E_r\{[ak_x/\pi + (m - n)]^2 + [ak_y/\pi + (m + n)]^2\}$, where $E_r = \hbar^2\pi^2/(2Ma^2)$ is the recoil energy. The off-diagonal matrix elements read

$$\begin{aligned}
\langle\vec{k}|H_0|\vec{k} + \vec{G}_{\pm1,0}\rangle &= -\frac{V_0}{4}\eta\epsilon(\cos\alpha e^{\mp i\theta} + e^{\pm i\theta}),\\
\langle\vec{k}|H_0|\vec{k} + \vec{G}_{0,\pm1}\rangle &= -\frac{V_0}{4}\eta(\cos\alpha e^{\pm i\theta} + \epsilon^2 e^{\mp i\theta}),\\
\langle\vec{k}|H_0|\vec{k} + \vec{G}_{\pm1,\mp1}\rangle &= -\frac{V_0}{4}\epsilon\cos\alpha,\\
\langle\vec{k}|H_0|\vec{k} + \vec{G}_{\pm1,\pm1}\rangle &= -\frac{V_0}{4}\epsilon\eta^2\cos\alpha.
\end{aligned} \tag{2}$$

We focus on the second band into which bosons are pumped [6]. There are four points in the Brillouin zone (BZ); namely, $O = (0,0)$, $K_{1,2} = (\pm\frac{\pi}{2a_0}, \frac{\pi}{2a_0})$, and $M = (\frac{\pi}{a_0}, \frac{\pi}{a_0})$, at which the Bloch wave functions are TR invariant and, thus, real valued. The band spectra are symmetric with respect to these points, which means that they are local energy extrema or saddle points. For the symmetric lattice with $\alpha = \alpha_0$, the second band has doubly degenerate energy minima of the states ψ_{K_1} and ψ_{K_2} located at K_1 and K_2, respectively. For the asymmetric case, the degeneracy between ψ_{K_1} and ψ_{K_2} is lifted. For $\alpha < \alpha_0$ ($\alpha > \alpha_0$), K_1 (K_2) becomes the band minimum. The energy spectrum of $\alpha = 0$ is shown in Figs. 2(a) and 2(b) (a similar energy spectrum with different parameters is plotted in Ref. [6]).

The real-space distributions of ψ_{K_1} and ψ_{K_2} are also calculated. Their nodal lines pass the centers of the deeper sites of A. Thus, the orbital component on the A sites is p type and that on the shallower sites of B is s type. In fact, the p orbital configurations of $\psi_{K_1}(\vec{r})$ and $\psi_{K_2}(\vec{r})$

in the A sites are actually not exactly along the directions of $\hat{e}_x \pm \hat{e}_y$ because of the lack of tetragonal symmetry. This point is mostly clear in the case of strong potentials so that we can define local orbitals on each site. Even for the symmetric lattice, the p_x and p_y orbitals on the A sites can be defined according to their parities under reflection with respect to the x axis. However, they are nondegenerate. The orbital components of $\psi_{K_1}(\vec{r})$ and $\psi_{K_2}(\vec{r})$ are nearly the same on A sites; that is, mostly the lower-energy p orbital is slightly hybridized with the higher one. The orthogonality of these two states comes from their different lattice momenta.

Interactions determine the configurations of UBEC in the presence of degenerate band minima. Any linear superposition among them gives rise to condensate wave functions with the same kinetic energy. However, interactions break this degeneracy. Previous studies on p orbital BECs based on tight-binding models predicted linear superpositions between two Bloch wave functions at degenerate band minima with a phase difference $\pm\frac{\pi}{2}$. Such a condensate breaks TR symmetry spontaneously [3,8]. Bosons on p orbital sites aggregate into the $p_x \pm ip_y$ states to reduce their repulsive interaction energy. This is a result of the second Hund rule: complex p orbitals are spatially more extended than the real orbitals and thus bosons have more room to avoid each other.

The optical potential in the current experiment is shallow; thus, the system is in the weak-correlation regime [6]. Instead of the tight-binding model, we use the GP equation. Because of the absence of the lattice potential along the z axis, we neglect the z dependence of the condensate wave function. We only consider its distribution $\Psi(\vec{r})$ in the xy plane. It is normalized as $\frac{1}{\Omega}\int' d^2r|\Psi(\vec{r})|^2 = 1$ where $\int' d^2\vec{r}$ integrates over one unit cell with the area of $\Omega = 2a_0^2$. The GP equation reads

$$\left\{-\frac{\hbar^2\vec{\nabla}^2}{2M} + V(\vec{r}) + g\rho_0|\Psi(\vec{r})|^2\right\}\Psi(\vec{r}) = E\Psi(\vec{r}), \tag{3}$$

where $\rho_0 = N_0/V$ is the average three-dimensional (3D) density, with N_0 being the total boson number in the condensate and V being the 3D volume of the system. g is the s-wave scattering interaction parameter. In the calculations below, various values of interaction parameters $g\rho_0$ are used from 0 up to E_r, which is of the same order of magnitude as the bandwidth. For this intermediate interaction, the GP equation is known to provide a good description of the system.

Although Eq. (3) looks the same as the usual GP equation, the marked difference is that $\Psi(\vec{r})$ is not the ground state condensate but the metastable one belonging to the second band. The nonlinearity of the GP equation allows mixing between different Bloch wave states. Let us start from the symmetric lattice with $\alpha = \alpha_0$. Equation (3) is solved

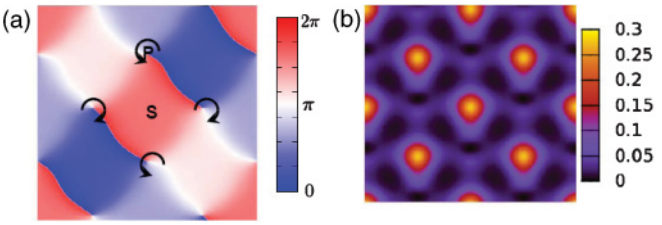

FIG. 3. (Color online) Distributions of (a) phase and (b) density patterns of complex UBEC. The parameter values are the same as in Fig. 1, except that $g\rho_0 = 0.6E_r$ and $\alpha = 36^\circ$. The vortex and antivortex cores are located in the centers of A sites.

self-consistently as follows: We define the renormalized potential as $V_{\rm eff}(\vec{r}) = V(\vec{r}) + g\rho_0|\Psi(\vec{r})|^2$ and solve the corresponding renormalized band structure. Then the condensate wave function is optimized to minimize the total energy, which in turn determines $V_{\rm eff}$. The renormalized band structure is similar to the free band structure, which still has two degenerate band minima at K_1 and K_2. We define the condensate wave function as

$$\Psi(\vec{r}) = \cos\delta\psi_{K_1}(\vec{r}) + e^{i\phi}\sin\delta\psi_{K_2}(\vec{r}). \tag{4}$$

The total energy reaches a minimum at $\delta = \frac{\pi}{4}$ and $\phi = \pm\frac{\pi}{2}$. Notice that the point $\phi = 0$ also represents a metastable stationary state which exhibits nontrivial dynamical instability [22–24], which is beyond the scope of our paper. These complex condensate wave functions only have nodal points, while the real ones ψ_{K_1} and ψ_{K_2} have nodal lines. The complex ones are spatially more uniform and thus are favored by interactions. We plot the phase and density patterns of this condensate in Fig. 3 , which exhibit a vortex-antivortex lattice structure. The vortex and antivortex cores are located alternatively at the centers of A sites, where the antiferromagnetic order of orbital angular momentum develops. For every closest-four B sites, their phases wind around the central A site following the same vorticity. This is similar to the case of the tight-binding models [3,8]. The Bragg peaks in the time of flight (TOF) spectra are located at $(m + \frac{1}{2})\vec{b}_1 + n\vec{b}_2$ and $m\vec{b}_1 + (n + \frac{1}{2})\vec{b}_2$ as observed in the experiment [6]. In particular, the four peaks of $\pm\frac{1}{2}\vec{b}_{1,2} = (\pm\frac{\pi}{2a_0}, \pm\frac{\pi}{2a_0})$ are strongest with equal intensities, as shown in Fig. 4(a).

Now we move to the asymmetric lattice whose free band structure minimum is nondegenerate. The complex condensates are favored by interactions and thus should be stable at sufficiently weak asymmetries. Certainly, at large asymmetries, the real condensate wins due to the gain of

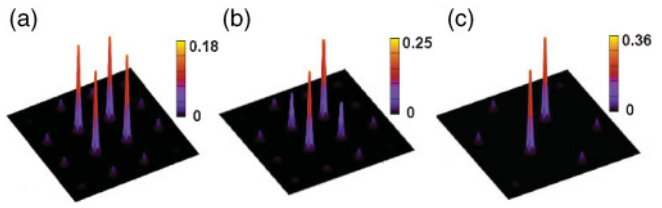

FIG. 4. (Color online) Density distribution in the time-of-flight spectrum for (a) complex condensate in the symmetric case ($\alpha = 36.0^\circ$), (b) complex condensate in the asymmetric case ($\alpha = 35.5^\circ$), and (c) real condensate ($\alpha = 34.5^\circ$). Other parameter values are the same as for Fig. 1, except for α.

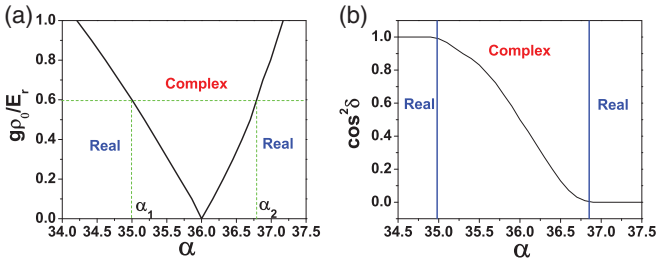

FIG. 5. (Color online) (a) Phase diagram as a function of α and interaction strength $g\rho_0$. Other parameters values are the same as for Fig. 2. (b) Condensate fractions of ψ_{K_1} in the complex UBEC $\Psi = \cos\delta\psi_{K_1} \pm i\sin\delta\psi_{K_2}$. The parameter values are the same as for Fig. 1 except for α and $g\rho_0 = 0.6E_r$.

band energy. This picture is explicitly confirmed by the phase diagram calculated by the GP equation. As shown in Fig. 5(a), for a given value of the interaction strength $g\rho_0$, the complex condensate in the form of Eq. (4) is stable in a finite parameter range from α_1 to α_2; beyond this regime the condensate changes to the real one, and the TOF spectra of such a real condensate only contain peaks of $(m + \frac{1}{2})\vec{b}_1$ or $(m + \frac{1}{2})\vec{b}_2$, as shown in Fig. 4(c)

In the complex condensate, the relative phase ϕ between ψ_{K_1} and ψ_{K_2} is always $\pm\frac{\pi}{2}$; that is, Ψ and Ψ^* are degenerate as TR partners; δ is asymmetry dependent. The spatial asymmetry of $|\Psi(\vec{r})|^2$ depends on that of the bare potential V. However, $V_{\rm eff}$, a combination of V and $|\Psi|^2$, becomes symmetric. Without loss of generality, $\Psi(\vec{r})$ is expanded in terms of two orthonormal real wave functions $\psi_1(\vec{r})$ and $\psi_2(\vec{r})$ in the same way as in Eq. (4) by replacing ψ_{K_1} (ψ_{K_2}) with ψ_1 (ψ_2). Apparently, both $\Psi(\vec{r})$ and $\Psi^*(\vec{r})$ satisfy Eq. (3) and yield the same $V_{\rm eff}$. The corresponding renormalized single particle Hamiltonian $-\hbar^2\nabla^2/(2M) + V_{\rm eff}$ has degenerate band minima ψ_1 and ψ_2. However, please note that the superposition principle does not apply to the nonlinear GP equation: ψ_1 and ψ_2 are not solutions to Eq. (3). $|\Psi(\vec{r})|^2$ is also asymmetric depending on the asymmetry of the bare potential V. The TOF spectra still exhibit four dominant peaks at $\pm(\frac{\pi}{2a_0}, \frac{\pi}{2a_0})$ and $\pm(-\frac{\pi}{2a_0}, \frac{\pi}{2a_0})$, as shown in Fig. 4(b). The relative intensities of these two pairs of peaks depend on the lattice asymmetry, which can be reflected by the condensation fractions ψ_{K_1} in the complex condensate, as plotted in Fig. 5(b). An observation of the asymmetric peaks at $\pm\frac{1}{2}\vec{b}_{1,2}$ for $\alpha_1 < \alpha < \alpha_2$ would provide supporting evidence for the complex condensates. The TOF spectra lack phase information; thus, the observation of the symmetric peaks $\pm\frac{1}{2}\vec{b}_{1,2}$ at α_0 [6] could be interpreted as the phase separation of real condensates of ψ_{K_1} or ψ_{K_2}, or an incoherent mixing between them. However, in these scenarios, the lattice asymmetry lifts the degeneracy and only leads to one pair of peaks. Even two condensates could coexist forming domains; the condensate fraction of ψ_{K_1} in the complex condensate should not follow that plotted in Fig. 5(b).

For a better understanding of phase transitions between real and complex UBEC, we construct the Ginzburg-Landau (GL) free energy as

$$F = -r_1|\Psi_{K_1}|^2 - r_2|\Psi_{K_2}|^2 + g_1|\Psi_{K_1}|^4 + g_2|\Psi_{K_2}|^4 + g_3|\Psi_{K_1}|^2|\Psi_{K_2}|^2 + g_4(\Psi^*_{K_1}\Psi^*_{K_1}\Psi_{K_2}\Psi_{K_2} + \text{H.c.}), \tag{5}$$

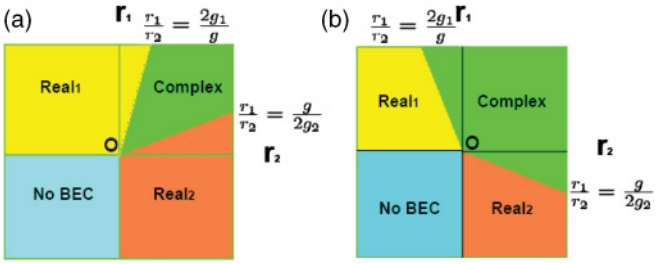

FIG. 6. (Color online) Phase diagram as a function of r_1 and r_2 predicted by Eq. (6) for (a) $g > 0$ and (b) $g < 0$.

where $\Psi_{K_1} = \psi_{K_1} e^{i\theta_1}$ and $\Psi_{K_2} = \psi_{K_2} e^{i\theta_2}$ describe the condensate order parameters at K_1 and K_2, respectively; θ_1 and θ_2 are the phases of the condensates of Ψ_{K_1} and Ψ_{K_2}, respectively, and ψ_1 and ψ_2 are real as explained before. Although Ψ_{K_1} and Ψ_{K_2} do not couple at the quadratic level due to the requirement of translational symmetry, they do couple at the quartic level as in the g_4 term because $\pm 2(\vec{K}_1 - \vec{K}_2)$ equals reciprocal lattice vectors. g_4 is positive for repulsive interactions, which favors the relative phase difference $\theta_1 - \theta_2 = \pm\frac{\pi}{2}$; thus, the free energy in Eq. (5) can be reduced to

$$F = -r_1\psi_{K_1}^2 - r_2\psi_{K_2}^2 + g_1\psi_{K_1}^4 + g_2\psi_{K_2}^4 + g\psi_{K_1}^2\psi_{K_2}^2, \quad (6)$$

in which $g = g_3 - 2g_4$. We define $G = 4g_1g_2 - g^2$ and $g_1, g_2, G > 0$ as required by the thermodynamic stability condition. In the superfluid regime, the complex UBEC is characterized by the nonzero values of both Ψ_{K_1} and Ψ_{K_2}, while the real BECs correspond to one of these values being zero. Without loss of generality, we fix g_1, g_2, and g and plot the phase diagram of the superfluid regime as a function of r_1 and r_2. As shown in Fig. 6 , for $g > 0$, the complex BECs occur when $\frac{g}{2g_2} < \frac{r_1}{r_2} < \frac{2g_1}{g}$, where both r_1 and r_2 are positive. It is interesting to notice that, for $g < 0$, the complex BEC can exist even if one channel is off critical ($r_1 < 0$ or $r_2 < 0$), which means that, in this case, the complex BEC is purely induced by interaction. A similar phase diagram has been proposed in a different context about a p-wave resonant Bose gas [25,26].

As the interaction increases, the system is brought into the Mott insulating regime. Nevertheless, at least in the weakly insulating regime, the suppression of the superfluidity ordering is due to phase fluctuations, and the magnitudes $|\Psi_{K_1}|$ and $|\Psi_{K_2}|$ remain nonzero. Although θ_1 and θ_2 are disordered such that $\langle\Psi_{K_1}\rangle = \langle\Psi_{K_2}\rangle = 0$, their relative phase $\theta_1 - \theta_2 = \pm\frac{\pi}{2}$. This indicates a TR-breaking order with a bilinear form of Ψ_{K_1} and Ψ_{K_2} as $L = i\langle\Psi_{K_1}^*\Psi_{K_2} - \Psi_{K_2}^*\Psi_{K_1}\rangle$ in the Mott insulating state. Its physical meaning here remains the staggered circulating currents; that is, these exotic Mott insulating states preserve the antiferromagnetic orbital angular momentum (OAM) order of the complex BECs but not the global phase coherence.

In summary, we studied the UBEC observed in the high orbitals bands reported in Ref. [6]. The unconventional condensate wave functions can be real and TR invariant with nodal lines, or complex breaking TR symmetric with nodal points. In both cases, translational symmetry is broken due to the nonzero condensation wave vectors; thus, these UBECs can be considered as unconventional supersolid states. The interplay between lattice asymmetry and interactions drives the transition between them.

We are grateful to A. Hemmerich for carefully reading our manuscript and insightful discussions. We also thank A. Hemmerich, C. Morais Smith, and O. Tieleman for pointing out a mistake in an earlier version about the order of the phase transition. Z.C. and C.W. are supported by NSF DMR-1105945 and the AFOSR-YIP program.

[1] R. P. Feynman, *Statistical Mechanics, A Set of Lectures* (Addison-Wesley Publishing Company, Boston, Massachusetts, 1972).
[2] R. B. Bapat and T. Raghavan, *Non-Negative Matrices and Applications* (Cambridge University Press, Cambridge, United Kingdom, 1997).
[3] C. Wu, Mod. Phys. Lett. B **23**, 1 (2009).
[4] J. Sebby-Strabley, M. Anderlini, P. S. Jessen, and J. V. Porto, Phys. Rev. A **73**, 033605 (2006).
[5] T. Müller, S. Fölling, A. Widera, and I. Bloch, Phys. Rev. Lett. **99**, 200405 (2007).
[6] G. Wirth, M. Ölschläger, and A. Hemmerich, Nature Phys. **7**, 147 (2011).
[7] M. Ölschläger, G. Wirth, and A. Hemmerich, Phys. Rev. Lett. **106**, 015302 (2011).
[8] W. V. Liu and C. Wu, Phys. Rev. A **74**, 13607 (2006).
[9] A. Isacsson and S. M. Girvin, Phys. Rev. A **72**, 053604 (2005).
[10] O. E. Alon, A. I. Streltsov, and L. S. Cederbaum, Phys. Rev. Lett. **95**, 030405 (2005).
[11] C. Wu, W. V. Liu, J. E. Moore, and S. Das Sarma, Phys. Rev. Lett. **97**, 190406 (2006).
[12] V. M. Stojanović, C. Wu, W. V. Liu, and S. Das Sarma, Phys. Rev. Lett. **101**, 125301 (2008).
[13] A. B. Kuklov, Phys. Rev. Lett. **97**, 110405 (2006).
[14] J.-P. Martikainen, Phys. Rev. A **83**, 013610 (2011).
[15] M. Lewenstein and W. V. Liu, Nature Phys. **7**, 101 (2011).
[16] C. Wu, D. Bergman, L. Balents, and S. Das Sarma, Phys. Rev. Lett. **99**, 70401 (2007).
[17] V. W. Scarola and S. Das Sarma, Phys. Rev. Lett. **95**, 033003 (2005).
[18] C. Xu and M. P. A. Fisher, Phys. Rev. B **75**, 104428 (2007).
[19] J. H. Challis, S. M. Girvin, and L. I. Glazman, Phys. Rev. A **79**, 043609 (2009).
[20] X. Li, E. Zhao, and W. V. Liu, Phys. Rev. A **83**, 063626 (2011).
[21] Q. Zhou, J. V. Porto, and S. Das Sarma, Phys. Rev. B **83**, 195106 (2011).
[22] V. S. Shchesnovich and V. V. Konotop, Phys. Rev. Lett. **102**, 055702 (2009).
[23] V. S. Shchesnovich, Phys. Rev. A **80**, 031601 (2009).
[24] V. S. Shchesnovich and V. V. Konotop, Phys. Rev. A **75**, 063628 (2007).
[25] S. Choi and L. Radzihovsky, e-print arXiv:1106.5765 (to be published).
[26] L. Radzihovsky and S. Choi, Phys. Rev. Lett. **103**, 095302 (2009).